



Nanoscale

**Bulk and surface exsolution produces a variety of Fe-rich and Fe-depleted ellipsoidal nanostructures in La<sub>0.6</sub>Sr<sub>0.4</sub>FeO<sub>3</sub> thin films**

Journal:	<i>Nanoscale</i>
Manuscript ID	NR-ART-09-2021-006121.R2
Article Type:	Paper
Date Submitted by the Author:	25-Nov-2021
Complete List of Authors:	SYED, KOMAL; University of California Irvine, Materials Science & Engineering Wang, Jiayue; Massachusetts Institute of Technology, Nuclear Science and Engineering Yildiz, Bilge; Massachusetts Institute of Technology, Bowman, William; University of California Irvine, Materials Science and Engineering

SCHOLARONE™  
Manuscripts

# 1 **Bulk and surface exsolution produces a variety of Fe-** 2 **rich and Fe-depleted ellipsoidal nanostructures in** 3 **La<sub>0.6</sub>Sr<sub>0.4</sub>FeO<sub>3</sub> thin films**

4  
5 Komal Syed<sup>1</sup>, Jiayue Wang<sup>2</sup>, Bilge Yildiz<sup>2,3</sup>, William J. Bowman<sup>1,4</sup>

6  
7 <sup>1</sup> Department of Materials Science & Engineering, University of California, Irvine, CA USA

8  
9 <sup>2</sup> Department of Nuclear Science and Engineering, Massachusetts Institute of Technology,  
10 Cambridge, MA USA

11  
12 <sup>3</sup> Department of Materials Science and Engineering, Massachusetts Institute of Technology,  
13 Cambridge, MA USA

14  
15 <sup>4</sup> Irvine Materials Research Institute, University of California, Irvine, CA USA

## 16 **Abstract**

17  
18  
19 The past several years have seen a resurgence in the popularity of metal exsolution as an approach  
20 to synthesize advanced materials proposed for novel catalytic, magnetic, optical, and  
21 electrochemical properties. Whereas most studies to-date have focused on surface exsolution  
22 (motivated by catalysis), we instead report on the diversity of nanostructures formed in  
23 La<sub>0.6</sub>Sr<sub>0.4</sub>FeO<sub>3</sub> thin films during sub-surface or so-called ‘bulk’ exsolution, in addition to surface  
24 exsolution. Bulk exsolution is a promising approach to tuning the functionality of materials, yet  
25 there is little understanding of the nanostructures exsolved within the bulk and how they compare  
26 to those exsolved at gas-solid interfaces. This work combines atomic- and nano-scale imaging and  
27 spectroscopy techniques applied using a state-of-the-art aberration-corrected scanning  
28 transmission electron microscope (STEM). In doing so, we present a detailed atomic-resolution  
29 study of a range of Fe-rich and Fe-depleted nanostructures possible *via* exsolution, along with  
30 qualitative and quantitative chemical analysis of the exsolved nanostructures and oxide phases  
31 formed throughout the film. Local structural changes in the perovskite matrix, coinciding with  
32 nanostructure exsolution, are also characterized with atomic-resolution STEM imaging. Fe  
33 exsolution is shown to create local A-site rich domains of Ruddlesden-Popper phase, and some  
34 stages of this phase formation have been demonstrated in this work. In particular, phase boundaries  
35 are found to be the primary nucleation sites for bulk and surface exsolution, and the exsolved  
36 particles observed here tend to be ellipsoidal with shape factor of 1.4. We report a range of  
37 nanostructure types (core-shell, bulk core-shell, adjacent, and independent particles), revealing  
38 several possible avenues of future exploration aimed to understand the formation mechanism of  
39 each exsolution type and to develop their functionality. This work is thus relevant to materials  
40 scientists and engineers motivated to understand and utilize exsolution to synthesize materials with  
41 predictable nanostructures.

42  
43  
44

## 1 Introduction

2  
3 Exsolution is an *in situ* synthesis method for creating highly-tunable catalytic nanostructures  
4 anchored in the surface of an oxide support<sup>1–7</sup>. This flexible nanocatalyst synthesis approach can  
5 produce active particles which are more durable than impregnated nanostructures, and which can  
6 be strained as a result of being partially submerged in the oxide – offering enhanced activity. Our  
7 current understanding of exsolution results from nearly two decades of catalysis research dating  
8 back to pioneering work on “self-regenerative” perovskite-supported precious metal (Pd, Rh and  
9 Pt) catalysts for automotive emissions control by researchers at Daihatsu<sup>1,8–12</sup>. Since then, a range  
10 of nanostructures have been developed for several catalytic applications, such as solid oxide  
11 fuel/electrolysis cells<sup>4,4,5,13–29</sup>, hydrogen and syngas production<sup>30–34,18,35–37</sup>, oxygen evolution<sup>38</sup>,  
12 CO<sub>2</sub> reduction<sup>39,40</sup>, and photocatalysis<sup>41</sup>. Very recently, focus has turned to engineering the bulk  
13 properties of functional oxides using the bulk exsolution design strategy, which, for instance have  
14 effectively tailored the electronic transport properties of a lanthanum ferrite perovskite<sup>42</sup>.

15 Exsolution, also called “self-regeneration” or “solid-state crystallization” is a phase  
16 decomposition reaction that involves metal cation coalescence at/near individual atomic-scale  
17 point defects of opposite charge, such as oxygen vacancies. This is often observed in the vicinity  
18 of extended defects like surfaces and grain boundaries due to the relatively lower vacancy  
19 formation energy. Li, Liu *et al.* reviewed progress in the field of exsolution-derived  
20 electrocatalysts through 2017, see Table 3 of<sup>2</sup>. Many compositions have been investigated, mainly  
21 with the goal of efficient use of precious metals and various transition metals (though mostly Ni  
22 or its alloys) selected for particular reactions. Transition metals (MnO<sup>3,26,43</sup>, Fe<sup>3,13,28,30,43–45</sup>, Fe-  
23 Co<sup>29</sup>, FeNi<sub>3</sub><sup>40</sup>, Fe-Ni<sup>17,30</sup>, Co<sup>24,25,43,46</sup>, Co-Ni<sup>25,47</sup>, Ni<sup>4,5,13–16,18,22,24,25,27,31–37,43,48–50</sup>, Ni-Cu<sup>32</sup>, Cu  
24 <sup>3,24,32</sup>, Re/Ni/Fe<sup>51</sup>, Ce<sup>3</sup>, Ag<sup>19</sup>, Rare-earth vanadates doped with transition metal<sup>24</sup>), noble metals  
25 (Pd<sup>1,10–12,23</sup>, Pt<sup>9,10,12,52</sup>, Ir<sup>38</sup>, Rh<sup>9,10,12,39,52,53</sup>, Ru<sup>20–22</sup>), and transition metal dichalcogenides (WS<sub>2</sub>  
26 <sup>41</sup>) have been widely studied for exsolution.

27 In terms of nanostructure morphology, the main focus has been surface-anchored  
28 nanostructures for catalysis; however, several researchers have also reported bulk (i.e., sub-  
29 surface) exsolution of embedded nanostructures<sup>54–56</sup>. Dai, Pan, *et al.* concluded based on *in situ*  
30 TEM studies of Rh exsolution from CaTiO<sub>3-δ</sub> that initial-stage exsolution created nanostructures  
31 embedded in the perovskite matrix, making them inaccessible during heterogeneous catalysis<sup>53</sup>.  
32 Kim, Choi, *et al.* reported STEM dark field images clearly showing bulk exsolution of Ni particles  
33 throughout the thickness of epitaxially grown La<sub>0.2</sub>Sr<sub>0.7</sub>Ti<sub>0.9</sub>Ni<sub>0.1</sub>O<sub>3-δ</sub> thin films, but did not  
34 interrogate these nanostructures beyond nanometer-scale energy dispersive spectroscopy (EDS)  
35 line profiles confirming the presence of Ni<sup>50</sup>. Han, Irvine, *et al.* showed as well that Ni exsolves  
36 in the bulk of epitaxial La<sub>0.2</sub>Sr<sub>0.7</sub>Ni<sub>0.1</sub>Ti<sub>0.9</sub>O<sub>3-δ</sub> thin films, and while they did not explore this, there  
37 is indication that various core-shell nanostructures formed in their films during/after Ni exsolution  
38 <sup>37</sup>. In the context of bulk exsolution, Kousi, Metcalfe, *et al.* demonstrated that submerged Ni  
39 nanoparticles exsolved from La<sub>0.8</sub>Ce<sub>0.1</sub>Ni<sub>0.4</sub>Ti<sub>0.6</sub>O<sub>3-δ</sub> strain the perovskite lattice upon oxidation to  
40 crystallographically-aligned NiO, yielding favorable oxygen exchange properties for methane  
41 conversion to syngas<sup>34</sup>.

42 Recent publications by co-authors of this study have been focused on Fe exsolution in  
43 La<sub>0.6</sub>Sr<sub>0.4</sub>FeO<sub>3</sub> (LSF) thin films<sup>6,42</sup>. Most recently, Wang *et al.* reported that Fe<sup>0</sup> exsolution in LSF  
44 results in major chemical and structural reorganization at the surface and also in the bulk, which  
45 can be used effectively to tailor electrical, magnetic and chemical properties of the resulting  
46 nanocomposite<sup>42</sup>. It was demonstrated that exsolution in LSF results in not only metallic iron

1 nanoparticles whose magnetization could be modulated, but also Ruddlesden-Popper domains and  
2 Fe-deficient percolating channels which facilitated an increase in electronic conductivity by over  
3 100 times<sup>42</sup>. Particularly, it was shown that the Fe-deficient percolating channels can enhance  
4 electronic conductivity by several orders of magnitude<sup>42</sup>. Such findings have direct implications  
5 for fabricating multifunctional nanocomposites for wide range of applications, making this LSF  
6 system valuable for exploring bulk and surface nanostructure morphology.

7 Here, we report a detailed-study of various Fe-based embedded nanostructures possible in LSF  
8 thin films *via* so-called bulk exsolution. LSF was chosen as a model perovskite system due to well-  
9 understood defect chemistry and the technological promise provided by its bulk properties in  
10 chemical looping, solid oxide cells, and facilitating magnetic nanostructures, as described in our  
11 recent study<sup>42</sup> which also includes discussion of the formation mechanism of the exsolved  
12 nanostructures in some detail. The aim of this work is to illustrate the variation in nanostructures  
13 that one can make in this material, which should help guide the design and synthesis of exsolved  
14 nanostructures in a broad range of chemical compositions, microstructures, and applications. We  
15 quantify the structural and chemical aspects of bulk exsolution using imaging and spectroscopy  
16 down to the atomic- and nanoscale using a state-of-the-art aberration-corrected STEM. There has  
17 not yet been a detailed study on the various types of nanostructures possible *via* bulk exsolution.  
18

## 19 **Methods**

20  
21 **LSF thin films were synthesized by PLD.** LSF powders were prepared by mixing and  
22 grinding La<sub>2</sub>O<sub>3</sub> (Sigma Aldrich, 99.999%), SrCO<sub>3</sub> (Sigma Aldrich, 99.995%), and Fe<sub>2</sub>O<sub>3</sub> (Alfa  
23 Aesar, 99.998%) powders in appropriate ratios, and then being calcined at 1000 °C for 5 hours.  
24 The powders are then pressed into a pellet with a hydrostatic press and sintered at 1350 °C for 20  
25 hours in stagnant air, thus yielding the target.

26 MgO (001) single crystal substrates (MTI Corporation, 1-side polished) were employed in this  
27 work. During pulsed laser deposition (PLD), the substrate temperature was kept at 850 °C in an  
28 oxygen pressure of 20 mTorr. By applying 30000 laser pulses (laser energy: 400 mJ) to the LSF  
29 target, an LSF thin film of ~120 nm thickness was grown on the substrate (substrate to target  
30 distance is 85 mm). This LSF film before exsolution will be referred to as ‘as-prepared LSF’ for  
31 rest of the article. After deposition, the sample was cooled in the deposition atmosphere at a cooling  
32 rate of 5 °C/min.

33 **Fe exsolution was induced by exposure to H<sub>2</sub>.** LSF sample is reduced in 0.5 Torr flushing  
34 H<sub>2</sub> at 400 °C for 0.5 hours to trigger exsolution.

35 **Atomic-scale imaging and chemical analyses were performed by aberration-corrected**  
36 **STEM - energy dispersive spectroscopy (EDS).** Exsolution in LSF was characterized using state-  
37 of-the-art aberration corrected JEOL Grand ARM300CF STEM operated at 300 keV. This  
38 instrument is equipped with dual silicon drift detectors for EDS with total detector area of 200  
39 mm<sup>2</sup>. The probe size was ~0.1 nm with a probe current of about 35pA. Low-background, high  
40 count analytical TEM holder was used to minimize any stray x-rays caused by holder. The film  
41 thickness of the exsolved LSF film (on MgO substrate) used in this study was measured to be ~165  
42 nm.

43 Gatan Microscopy Suite (GMS version 3) software was utilized for STEM-EDS mapping and  
44 analysis using the following EDS peaks: O *K<sub>α</sub>* (0.52 keV), Fe *K<sub>α</sub>* and *K<sub>β</sub>* (6.40 keV and 7.06 keV  
45 respectively), La *L<sub>α</sub>* and *L<sub>β</sub>* (4.65 keV and 5.04 keV and respectively), and Sr *K<sub>α</sub>* and *K<sub>β</sub>* (14.16  
46 keV and 15.84 keV respectively). Net counts for EDS elemental maps were obtained after doing

1 background subtraction using Kramers filter (with scaling option available in Gatan to better align  
2 the measured background to the original data). Due to sample drift observations during some EDS  
3 scans, aspect ratio for the EDS maps was accordingly adjusted to match the original STEM image.  
4 To interpret the chemistry of exsolved nanostructures in LSF, Cliff-Lorimer method<sup>57-59</sup> was used  
5 to calculate concentrations of cations, Fe, La and Sr. Due to the widely known limitations of  
6 quantification of light elements by EDS, we excluded O from quantitative analysis in this study.  
7 Experimental k-factors were calculated using the as-prepared LSF film as reference, since the  
8 stoichiometric composition of homogeneous LSF film is known.

9 Additional physical, chemical, and functional characterization methods (atomic force  
10 microscopy, X-ray diffraction, X-ray photoelectron spectroscopy, X-ray absorption spectroscopy,  
11 electrochemical impedance spectroscopy, finite element analysis, and vibrating-sample  
12 magnetometry) are detailed elsewhere<sup>42</sup>.

## 14 Results and Discussion

16 **STEM-EDS characterization of bulk and surface nanostructures.** The variety of  
17 nanostructures formed in LSF via exsolution are comprised of Fe-rich and Fe-depleted regions,  
18 accompanied by variation in La and Sr content (Fig. 1)<sup>42</sup>. Using STEM high-angle annular dark  
19 field (HAADF) and bright field (BF) imaging, we characterized LSF film on (001) MgO substrate  
20 before (Fig. 1a-c) and after exsolution (Fig. 1 d-f). After the treatment to trigger exsolution, LSF  
21 film shows distinct variety of nanostructures and oxide phases formed throughout the film (Figs.  
22 1d-f). We also observe the formation of Ruddlesden-Popper (RP) phase after exsolution; RP is a  
23 perovskite-like derivative with A-site rich domains and is quantified by a local translation of the  
24  $ABO_{3-\delta}$  structure by  $\sqrt{1/2}$  of a unit cell. Using EDS elemental mapping, we show that most Fe-  
25 rich exsolved particles correspond to La and Sr depletion (Fig. 1g). There is also variation observed  
26 in La and Sr signal, compared to the LSF film matrix, for regions which are depleted in Fe.

27 We observe four main categories of nanostructures formed via surface and bulk exsolution: (i)  
28 surface core-shell, (ii) bulk core-shell, (iii) adjacent particles, and (iv) independent particles (Fig.  
29 2). We demonstrated in our recent paper using FFT analysis that the bulk exsolved particles are in  
30 fact metallic Fe, while the surface exsolved particles are Fe oxide (either  $Fe_3O_4$  or  $\gamma-Fe_2O_3$ )<sup>42</sup> due  
31 to exposure to air after exsolution<sup>42</sup>. We observe majority of nanostructures to be exsolved at  
32 interfaces in the LSF film indicating the activation energy of Fe nucleation is likely lower at the  
33 interfaces. The core-shell structures of surface and bulk particles, both exsolved at phase  
34 boundaries of perovskite matrix and RP phase, can be seen in STEM HAADF and BF images  
35 (Figs. 2a-f). STEM HAADF images display Z-contrast, with the image intensity being proportional  
36 to the mean atomic number  $Z^n$  (where  $n \sim 1.7$ )<sup>60</sup>. STEM BF images, on the other hand, show phase  
37 and diffraction contrast<sup>61</sup>. To highlight the complementary information provided by both methods,  
38 the difference between perovskite matrix and RP phase domains is more apparent in STEM BF  
39 images (phase and diffraction contrast), while the STEM HAADF images display Z-contrast  
40 making it easier to differentiate between Fe-rich and Fe-depleted particles.

41

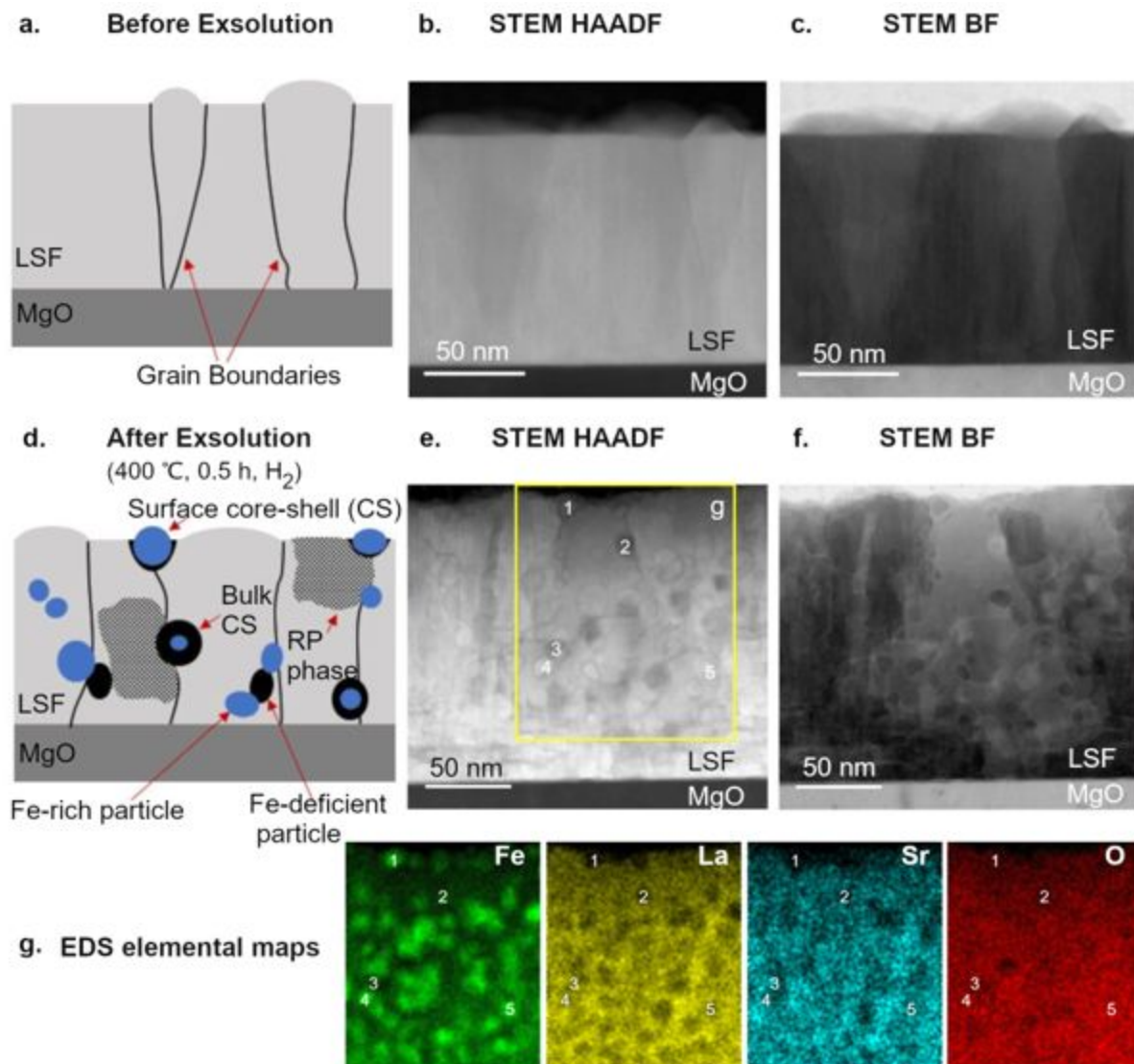


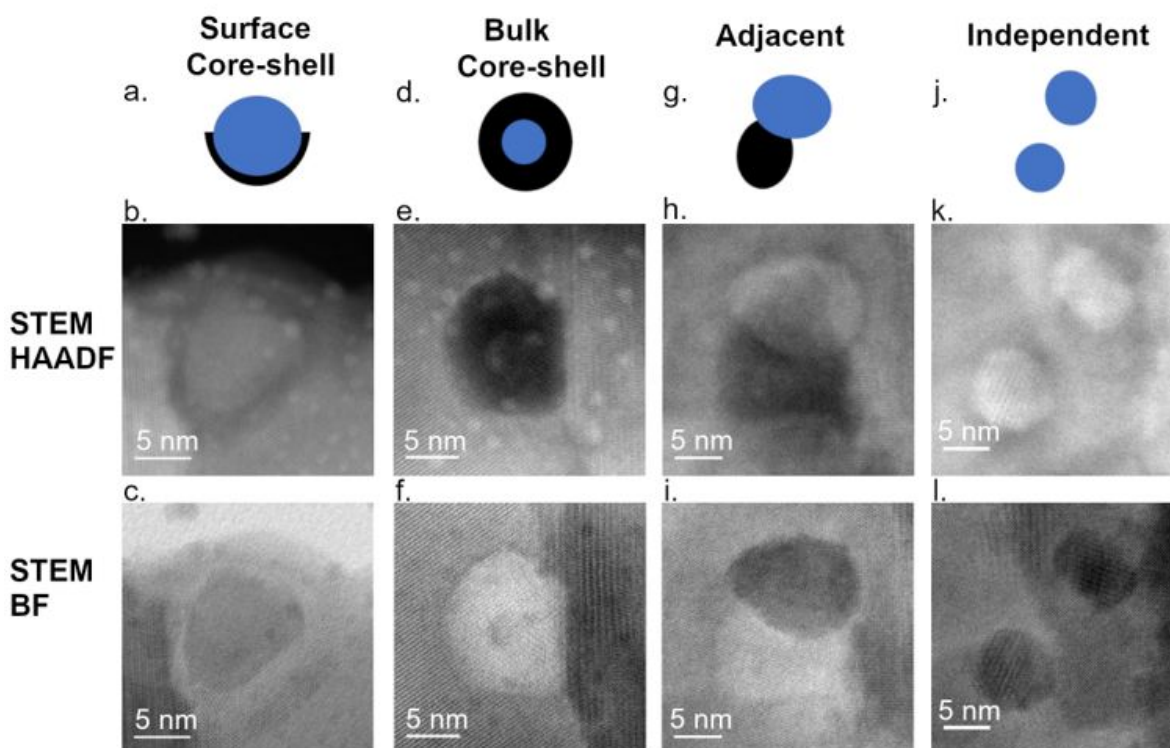
**Fig. 1:**  $\text{La}_{0.6}\text{Sr}_{0.4}\text{FeO}_3$  (LSF) thin films were deposited by pulsed laser deposition (PLD) on 001-oriented MgO single crystals (a) and analyzed using scanning TEM (STEM) high-angle annular dark field (HAADF) images (b) and STEM bright-field (BF) images (c). Treatment of the films in 0.5 torr  $\text{H}_2$  at 400°C for 0.5 h induced Fe exsolution, yielding a variety of Fe-rich and Fe-depleted nanostructures and oxide phases through the film depth (d-f). EDS elemental maps (net counts) of Fe K, La L, Sr Ka and O K showing Fe exsolution throughout the LSF film (g).

The core of the surface particle is rich in Fe, while the shell has primarily Fe and La signals suggesting presence of La/Fe based oxide, which is confirmed from quantitative analysis in the next section (Fig. 3b; see supplementary information Figs. S1-S3 for individual EDS elemental maps). Because the STEM data are two-dimensional projections of a three-dimensional object, it is ambiguous at times to distinguish the nanostructure from the surrounding matrix. Similarly, the bulk core-shell particle also has an Fe-rich core (Fig. 3d).

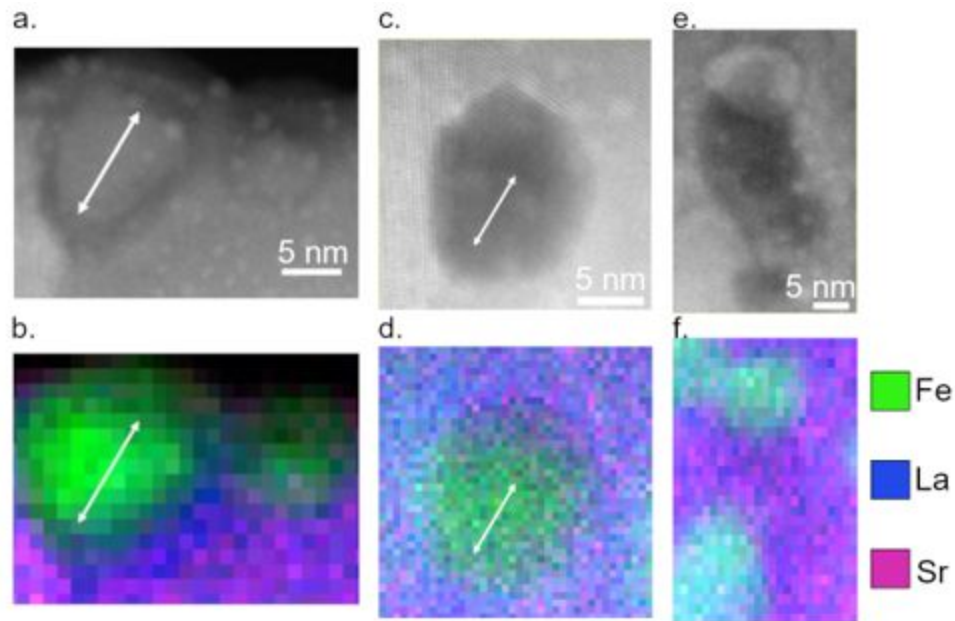
‘Adjacent particles’ are defined as nanostructures that are adjacent to each other after exsolution, with distinct high and low Z contrast in STEM HAADF imaging as well as phase/diffraction contrast in STEM BF imaging (Fig. 2h-i). These adjacent particles correspond to Fe-rich particles in the bulk resulting in Fe-depleted regions in the immediate vicinity (Fig. 3e-f).

1 Such adjacent particles are observed throughout the LSF film after exsolution, and more examples  
 2 can be seen in Fig. 4.

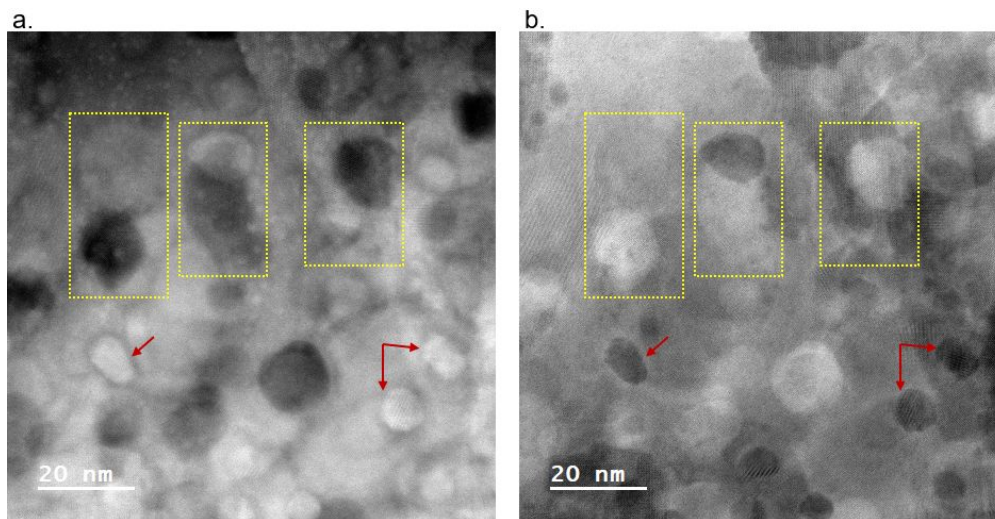
3 'Independent particles' are Fe-rich particles with no considerable Fe-depleted region nearby  
 4 (Fig. 2 j-l). These particles are also formed throughout the film via bulk exsolution (Fig. 4). These  
 5 independent particles have a very thin shell (~1-2 nm) which appears dark in Z-contrast images  
 6 (Fig. 4a), suggesting chemistry like the shell of bulk core-shell particles characterized earlier.  
 7 However, we categorized these particles as independent because clearly the Fe-rich 'core' region  
 8 comprises of majority of the particle, unlike the bulk core-shell particle where both core and shell  
 9 are prominently observed.  
 10



11  
 12 **Fig. 2:** Different types of Fe-based nanostructures observed in LSF thin film via exsolution shown using  
 13 schematics, STEM HAADF images and STEM BF images. Surface core-shell (a-c) and bulk core-shell  
 14 (d-f) structures have Fe-rich core and Fe-depleted shell. Another observed nanostructure is adjacent Fe-rich  
 15 and Fe-depleted particles (g-i). Independent Fe-rich nanostructures (without adjacent Fe-depleted regions)  
 16 are also observed throughout the LSF film (j-l).  
 17



1  
2 **Fig. 3:** STEM-HAADF images and overlay of EDS elemental maps (net counts) of surface core-shell  
3 particle (a-b), bulk core-shell (c-d) and adjacent particles (e-f).  
4

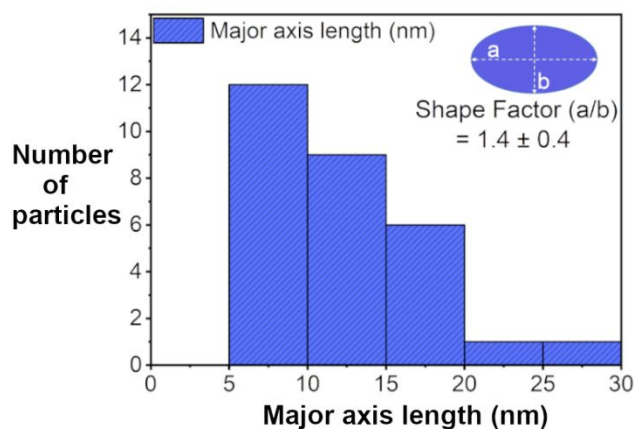


5  
6 **Fig. 4:** STEM HAADF (a) and BF (b) images showing variety of ‘adjacent’ Fe-rich and Fe-depleted  
7 particles observed, some marked with yellow outline. ‘Independent’ Fe-rich particles are marked with red  
8 arrows.  
9

10 **Geometry of exsolved nanostructures in LSF.** The Fe-rich nanostructures formed  
11 throughout the LSF film, both at surface and in bulk, are mostly observed to have ellipsoidal  
12 geometry. Most research studies to-date performed in  $H_2$  (e.g.  $H_2/Ar$ ) reducing environments, but  
13 focused only on surface exsolution, have also shown similar ellipsoidal or quasi-spherical  
14 geometry for exsolved particles<sup>16,36,62</sup>. Our results are thus consistent with the previous  
15 observations of surface particle geometry produced by  $H_2$  environments, but we further  
16 demonstrate that the bulk exsolved particles also have similar ellipsoidal geometry. Neagu *et al.*  
17<sup>36</sup> showed that the shape of the exsolved nanostructures can be tuned for various applications by  
18 changing the atmosphere for exsolution treatment as they explored with faceted particle growth in



1 a vacuum environment. Our results show that both surface and bulk exsolved particles will likely  
 2 maintain similar geometry depending on the exsolution treatment. For the exsolved particles in  
 3 this study, the shape factor (ratio of major axis length to minor axis,  $a/b$ ) was calculated to be  $1.4$   
 4  $\pm 0.4$  using  $\sim 30$  particles (see Fig. S4 in supplementary information). On average, the size of Fe-  
 5 rich nanostructures is  $12.1 \pm 4.8$  nm (Fig. 5). We don't observe any significant variation in particle  
 6 size with respect to the depth of the film.



9  
 10 **Fig. 5:** Particle size distribution of Fe-rich nanostructures (based on major length 'a') formed throughout  
 11 the LSF film via bulk exsolution.

12  
 13 The fact that the exsolved particles can be ellipsoidal points to the possibility of further designing this  
 14 property through spatially orienting the particles. One might wish to orient the major axis of the ellipsoids  
 15 to be parallel, perpendicular, or random, and this work would be foundational to developing such a future  
 16 hypothesis. An example of functionality related to spatial orientation and vicinity of the produced  
 17 nanostructures is electronic transport, wherein orienting the major axes of the particles in a parallel fashion  
 18 could provide a more direct percolating pathway from particle-to-particle, thus enhancing conductivity  
 19 through the particles. Alternatively, if the particles were designed for light absorption and/or scattering, it  
 20 could be beneficial to orient their major axis parallel to incident illumination for optimal photon coupling.

21  
 22 **Quantitative analysis of bulk and surface nanostructures.** The elemental compositional  
 23 analysis for the various nanostructures demonstrates that the exsolution of Fe directly affects the  
 24 nearby regions in the film. We observe two main phenomena with quantitative analysis: (a)  
 25 formation of lanthanum ferrite or  $\text{La}_x\text{Fe}_y\text{O}_{3-\delta}$  (LFO) around Fe particles because of reaction with  
 26 the LSF matrix, and (b) formation of Fe-depleted LSF adjacent to many Fe particles. Extracting  
 27 the absolute composition of the various Fe-based nanostructures is challenging due to unavoidable  
 28 contribution from the LSF matrix through the thickness of TEM lamellae specimen. However,  
 29 useful results were obtained on the relative compositional changes between the exsolved  
 30 nanostructures and the matrix. We quantified the concentration of cations using the Cliff-Lorimer  
 31 method<sup>57-59</sup>.

32 The surface core-shell particle is rich in Fe and depleted in both La and Sr, compared to the  
 33 LSF matrix (Fig. 6a). There is a decrease in HAADF intensity at the 'shell' region of the particle  
 34 (points 1 and 4). Points 2 and 3 correspond to the particle core region, while point 5 corresponds  
 35 to the LSF matrix. Point 2 corresponds to about 97 at% Fe, demonstrating that the core of the  
 36 particle is Fe-based only<sup>42</sup>. The gradual increase of La content and negligible change in Sr content,  
 37 from the core to shell region, indicate that the Fe core is surrounded by LFO. Considering the sum

1 of all cation concentrations to be 100 at%, the LSF matrix (as prepared) correspond to 50 at% Fe,  
 2 30 at% La and 20 at% Sr. Here, the LSF matrix region is 36.5 at% Fe, 42.4 at% La and 21.1 at%  
 3 Sr (Fig. 6a, point 5). This indicates that exsolution of the surface Fe particle resulted in depletion  
 4 of Fe in the surrounding perovskite matrix.

5 Although the contribution of the LSF matrix is more prominent in the bulk core-shell particle,  
 6 our analysis suggests that the core is Fe-rich and the shell is made of LFO like the surface particle,  
 7 Fig. 6b. We observe local increase in HAADF intensity corresponding to the core of bulk core-  
 8 shell particle (point1, Fig. 6b). Like the surface particle, the core is rich in Fe and depleted in La  
 9 and Sr. The increasing concentration of La in the shell region (between points 2 and 3, Fig. 6b),  
 10 while the Sr concentrations remains similar, indicates that the shell is made of LFO. This is like  
 11 the observation made for the surface particle.

12 The quantitative results from adjacent particles show that exsolution of Fe in the LSF film can  
 13 result in Fe-depleted LSF in the immediate vicinity of the Fe particles, Fig. 6c. The increase in  
 14 HAADF intensity (point 2, Fig. 6c) corresponds to the position of the Fe particle, while the  
 15 decrease in HAADF intensity (point 3, Fig. 6c) corresponds to the Fe-depleted particle. Going  
 16 from the bright to dark particle, the Fe concentration gradually decreases while La and Sr  
 17 concentrations gradually increase. However, the increase in Sr concentration is less prominent than  
 18 La. We don't observe an increase in Fe concentration at the onset of the bright particle (between  
 19 points 1 and 2, Fig. 6c) due to contribution from another superpositioned Fe-exsolved particle; the  
 20 particle is slightly out of focus in the HAADF image but within the interaction volume.  
 21 Furthermore, consistent La and Sr concentrations along the bright particle suggests it is the  
 22 contribution from LSF matrix.

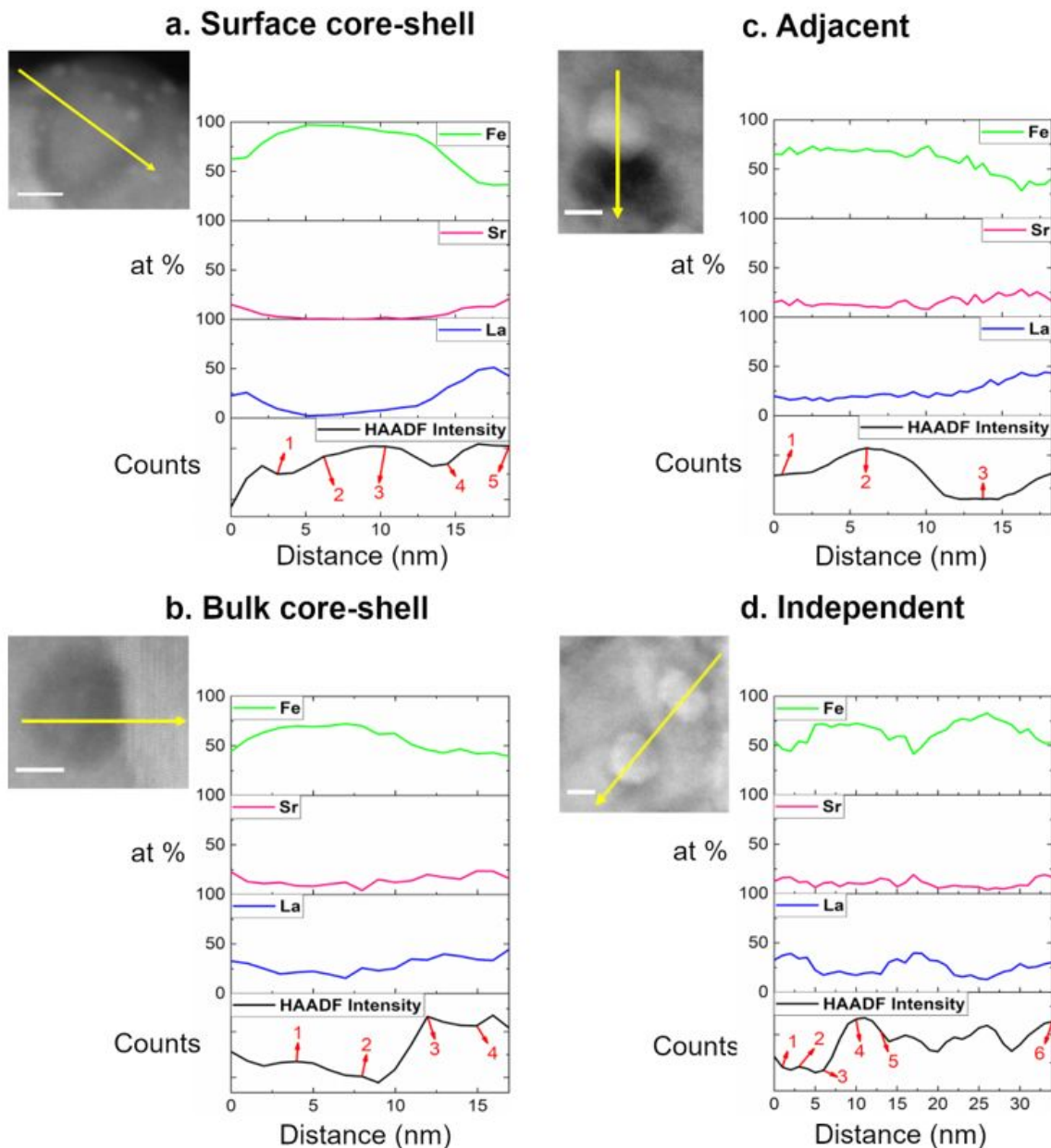
23 The quantitative analysis of independent particles confirms our hypothesis in the previous  
 24 section that the composition of these particles is like bulk core-shell particles, with a primarily Fe  
 25 'core' region and thin LFO 'shell' (Fig. 6d). The Fe core location corresponds to a local maximum  
 26 in HAADF intensity (point 4, Fig. 6d), and a plateau in the Fe content profile (5 nm – 15 nm). The  
 27 relatively consistent La and Sr content within the particle (between points 3 and 5, Fig. 6d) is  
 28 attributed to the LSF matrix concentration within the interaction volume. The elemental  
 29 concentrations in the LSF matrix region are 52.7 at% Fe, 30.4 at% La and 16.9 at% Sr (point 1,  
 30 Fig. 6d). Like the observation of the bulk core-shell particle, the La content increases going from  
 31 the core to shell region (point 3 to 2, Fig. 6d), whereas the Sr signal remains unchanged, showing  
 32 the presence of LFO shell around the independent particles. This is also evident by the dark  
 33 contrast around the Fe-rich particles in the HAADF image of Fig. 6d.

34 The dark HAADF contrast of the LFO shell formed around the Fe particles (Fig. 6) suggests  
 35 lower mean Z compared to the LSF film matrix, but can also be due to structural distortion at phase  
 36 boundaries affecting the HAADF signal. Mean Z for a compound can be calculated using different  
 37 methods; we used the following to estimate mean Z values<sup>63</sup>:

$$38 \quad Z = \sqrt{\sum_{i=1}^n a_i Z_i^2}$$

39 where,  $a_i$  is the atomic fraction and  $Z_i$  is the atomic number of the constituent elements. Mean  
 40 Z for LaFeO<sub>3</sub> and LSF are calculated to be 28.7 and 26.1 respectively. Since LaFeO<sub>3</sub> has higher  
 41 mean Z than LSF, the shell would have a higher HAADF signal than the matrix if it was composed  
 42 of LaFeO<sub>3</sub>, which is not the case here. Thus, we can assume that La:Fe ratio is not 1:1 in the shell.  
 43 Based on our quantitative analysis of shell regions as well as mean Z calculations, we believe the  
 44 shell around the Fe particles to be a La-depleted and Fe-rich (perovskite-like) oxide, compared to  
 45 the LSF matrix. The core-shell nature of some nanostructures could, for example, be leveraged in

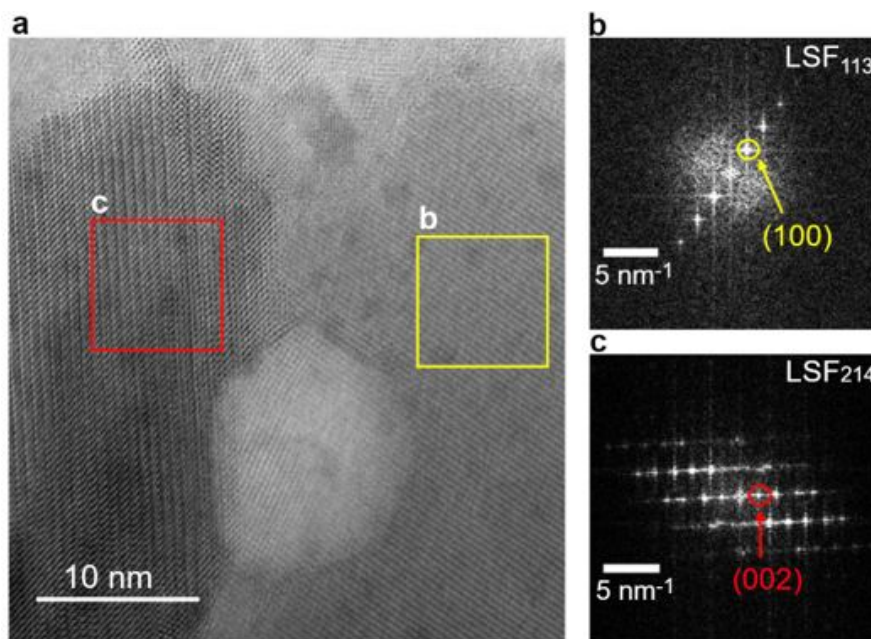
1 a situation where one wishes to tune a film's magnetic properties. In this case a variable to optimize  
 2 is the thickness of the oxide shell and thus the volumetric ratio of metal core to metal oxide shell.  
 3



4 **Fig. 6:** STEM-HAADF images and line profiles showing HAADF image intensity (counts) and elemental  
 5 concentration (at%) of cations Fe, La, and Sr across surface core-shell (a), bulk core-shell (b), adjacent (c),  
 6 and independent particles (d). Scale bar in HAADF images is 5 nm.  
 7  
 8

9 **Formation of Ruddlesden-Popper phase (LSF<sub>214</sub>) via bulk exsolution.** STEM  
 10 characterization and FFT analysis confirm that Fe exsolution in the LSF film creates local A-site  
 11 rich domains of RP phase. The general formula of RP phase can be given by  $A_{n+1}B_nO_{3n+1}$ ; i.e.  
 12  $A_2BO_4$  for  $n=1$ <sup>64</sup>. We found an inhomogeneous distribution of RP phases throughout the LSF film.  
 13 XRD results, detailed elsewhere<sup>42</sup>, showed that perovskite LSF continues to be the dominant phase  
 14 after exsolution with chemical expansion in the LSF lattice due to formation of oxygen vacancies.

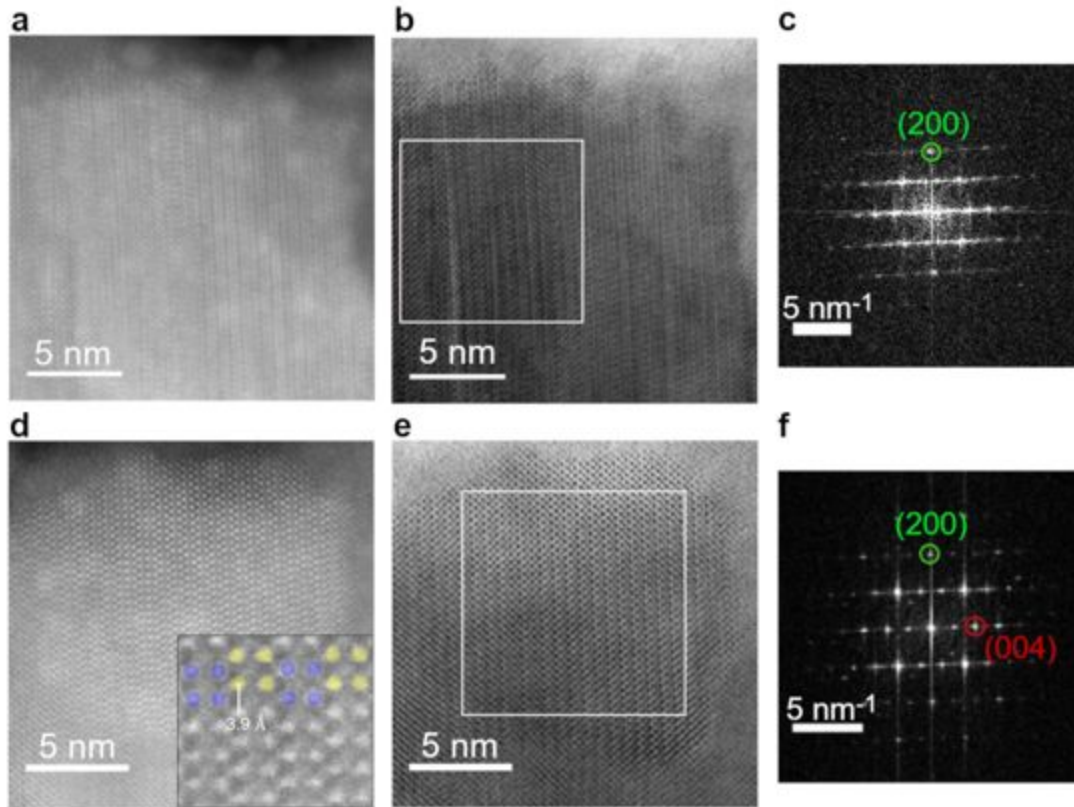
1 Many Fe nanostructures are observed to form at the boundaries of the LSF perovskite matrix and  
 2 RP phases. Fig. 7a shows a bulk core-shell particle formed at the phase boundary between the  
 3 original perovskite matrix (LSF<sub>113</sub>) and RP phase (LSF<sub>214</sub>) (Fig. 7).  
 4



5  
 6 **Fig. 7:** STEM-BF image (a) and FFT patterns of LSF<sub>113</sub> and LSF<sub>214</sub> respectively (b-c).  
 7

8 In the same specimen, we observe different stages of RP phase formation near the surface of  
 9 the LSF film (Fig. 8). For the partially transformed phase (Fig. 8a-b), (200) planes with non-  
 10 uniform linear contrast appear to be connected by zig-zag patterns, which is attributed to  
 11 disordered planar defects<sup>65</sup>. These planar-like defects are manifested as horizontal streaking on  
 12 the FFT pattern (Fig. 8c). In the fully transformed RP phase (Fig. 8d-e), we see well-ordered  
 13 arrangement of planar defects, shifted by  $\frac{1}{2}a[100]$  as can be seen clearly in the inset of the HAADF  
 14 image (Fig. 8d). Such ordered planar defects are commonly observed in A-site rich oxides, and  
 15 have been discussed previously by Suzuki *et al.*<sup>65</sup> This results in sharp FFT spots, along with  
 16 superlattice spots, as shown in Fig. 8f.

17 RP phase formation (simultaneous to Fe-exsolution) was also observed in a model epitaxial  
 18 thin-film LSF (~20nm) [see details in supplementary section, Fig. S5]. The characterization of  
 19 surface exsolution for this thin-film LSF has been previously published<sup>6</sup>. Our results on both the  
 20 thick LSF film (~165 nm) and thin LSF film (~20 nm) confirm that with modifications in  
 21 exsolution treatments, the formation of RP phase can be controlled to optimize exsolution of  
 22 catalytic particles and thus achieve improved catalytic efficiency.  
 23  
 24



1  
2 **Fig. 8:** Observation of two different stages of the RP phase formation via exsolution process shown with  
3 STEM HAADF images (a,d) and STEM BF images (b,e). Corresponding FFT patterns (c,f) are also shown.  
4 The yellow and purple circles in Fig. 8d highlight the shift of atomic columns in the fully transformed RP  
5 phase.  
6

## 7 **Conclusions**

8 We report four distinct types of Fe-based nanostructures formed in LSF thin films (on MgO  
9 substrate) via bulk and surface exsolution: surface core-shell, bulk core-shell, adjacent and  
10 independent nanostructures. The core-shell particles are determined to have a metallic Fe core and  
11 LFO shell. The adjacent nanostructures are Fe exsolved particles with Fe-depleted LSF in their  
12 immediate vicinity. The independent nanostructures are found to have the same structure and  
13 chemistry like the bulk core-shell particles, but with a prominent Fe core region and very thin ~  
14 1-2 nm LFO shell. The exsolved bulk and surface particles have a shape factor of 1.4. We show  
15 that Fe exsolution creates local A-site rich domains of RP phase and two different stages of this  
16 phase formation via exsolution process is captured and analyzed using STEM imaging in this work.  
17 The phase boundaries, such as between RP phase and perovskite matrix, are attributed to be the  
18 primary sites for surface and bulk exsolution, suggesting the activation energy of Fe nucleation is  
19 lower at these boundaries. This work presents an in-depth nanostructure-based analysis of bulk  
20 and surface exsolution in thin films, offering a beneficial guide for scientists and engineers  
21 interested in exploring exsolution to optimize advanced materials. In the future it would be  
22 valuable to systematically investigate the impact of film synthesis and processing conditions on  
23 the amount of each nanostructure type, to establish more predictive synthesis protocols for each  
24 type of nanostructure. This should point the way forward towards designing and realizing tunable  
25 functional materials containing a specific subset of the nanostructures presented here.

## 1 Acknowledgements

2 KS acknowledges support from US Department of Education Graduate Assistance in Areas of  
3 National Need (GAANN) Fellowship. WJB acknowledges support from the UCI new faculty start-  
4 up funding. For STEM-EDS characterization, the authors acknowledge the use of facilities and  
5 instrumentation at the UC Irvine Materials Research Institute (IMRI), which is supported in part  
6 by the National Science Foundation through the UC Irvine Materials Research Science and  
7 Engineering Center (MRSEC DMR-2011967). J.W. and B.Y. would like to thank the Exelon  
8 Corporation and the MIT Energy Initiative Seed Fund Program for supporting the work presented  
9 in this paper.

## 10 11 Conflict of Interest

12 None.

## 13 14 Author Contributions

15 WJB and KS designed the study. JW prepared the thin films. KS conducted the STEM  
16 characterization and data analysis. KS wrote the manuscript and all authors contributed to  
17 editing/revision. WJB supervised the project.

## 18 19 References

- 20 1. Nishihata, Y. *et al.* Self-regeneration of a Pd-perovskite catalyst for automotive emissions  
21 control. *Nature* **418**, 164–167 (2002).
- 22 2. Li, Y. *et al.* Controlling cation segregation in perovskite-based electrodes for high electro-  
23 catalytic activity and durability. *Chem. Soc. Rev.* **46**, 6345–6378 (2017).
- 24 3. Neagu, D., Tsekouras, G., Miller, D. N., Ménard, H. & Irvine, J. T. S. In situ growth of  
25 nanoparticles through control of non-stoichiometry. *Nat. Chem.* **5**, 916–923 (2013).
- 26 4. Myung, J., Neagu, D., Miller, D. N. & Irvine, J. T. S. Switching on electrocatalytic activity in  
27 solid oxide cells. *Nature* **537**, 528 (2016).
- 28 5. Zhu, T., Troiani, H. E., Mogni, L. V., Han, M. & Barnett, S. A. Ni-Substituted Sr(Ti,Fe)O<sub>3</sub>  
29 SOFC Anodes: Achieving High Performance via Metal Alloy Nanoparticle Exsolution. *Joule*  
30 **2**, 478–496 (2018).

- 1 6. Wang, J. *et al.* Tuning Point Defects by Elastic Strain Modulates Nanoparticle Exsolution on  
2 Perovskite Oxides. *Chem. Mater.* **33**, 5021–5034 (2021).
- 3 7. Rosen, B. A. Progress and Opportunities for Exsolution in Electrochemistry. *Electrochem* **1**,  
4 32–43 (2020).
- 5 8. Takehira, K. Highly Dispersed and Stable Supported Metal Catalysts Prepared by Solid Phase  
6 Crystallization Method. *Catal. Surv. Asia* **6**, 19–32 (2002).
- 7 9. Tanaka, H. *et al.* Self-Regenerating Rh- and Pt-Based Perovskite Catalysts for Automotive-  
8 Emissions Control. *Angew. Chem. Int. Ed.* **45**, 5998–6002 (2006).
- 9 10. Tanaka, H. *et al.* The intelligent catalyst having the self-regenerative function of Pd, Rh and  
10 Pt for automotive emissions control. *Catal. Today* **117**, 321–328 (2006).
- 11 11. Tan, I. *et al.* The Self-Regenerative ‘Intelligent’ Catalyst for Automotive Emissions Control.  
12 *Key Engineering Materials* <https://www.scientific.net/KEM.317-318.833> (2006)  
13 doi:10.4028/www.scientific.net/KEM.317-318.833.
- 14 12. Taniguchi, M. *et al.* The self-regenerative Pd-, Rh-, and Pt-perovskite catalysts. *Top. Catal.*  
15 **42**, 367–371 (2007).
- 16 13. Tsekouras, G., Neagu, D. & Irvine, J. T. S. Step-change in high temperature steam electrolysis  
17 performance of perovskite oxide cathodes with exsolution of B-site dopants. *Energy Environ.*  
18 *Sci.* **6**, 256–266 (2012).
- 19 14. Arrivé, C., Delahaye, T., Joubert, O. & Gauthier, G. Exsolution of nickel nanoparticles at the  
20 surface of a conducting titanate as potential hydrogen electrode material for solid oxide  
21 electrochemical cells. *J. Power Sources* **223**, 341–348 (2013).
- 22 15. Park, B. H. & Choi, G. M. Ex-solution of Ni nanoparticles in a  $\text{La}_{0.2}\text{Sr}_{0.8}\text{Ti}_{1-x}\text{Ni}_x\text{O}_{3-\delta}$   
23 alternative anode for solid oxide fuel cell. *Solid State Ion.* **262**, 345–348 (2014).

- 1 16. Neagu, D. *et al.* Nano-socketed nickel particles with enhanced coking resistance grown *in situ*  
2 by redox exsolution. *Nat. Commun.* **6**, 8120 (2015).
- 3 17. Liu, S., Liu, Q. & Luo, J.-L. Highly Stable and Efficient Catalyst with In Situ Exsolved Fe–Ni  
4 Alloy Nanospheres Socketed on an Oxygen Deficient Perovskite for Direct CO<sub>2</sub> Electrolysis.  
5 *ACS Catal.* **6**, 6219–6228 (2016).
- 6 18. Gao, Y., Chen, D., Saccoccio, M., Lu, Z. & Ciucci, F. From material design to mechanism  
7 study: Nanoscale Ni exsolution on a highly active A-site deficient anode material for solid  
8 oxide fuel cells. *Nano Energy* **27**, 499–508 (2016).
- 9 19. Zhu, Y. *et al.* Promotion of Oxygen Reduction by Exsolved Silver Nanoparticles on a  
10 Perovskite Scaffold for Low-Temperature Solid Oxide Fuel Cells. *Nano Lett.* **16**, 512–518  
11 (2016).
- 12 20. Madsen, B. D., Kobsiriphat, W., Wang, Y., Marks, L. D. & Barnett, S. A. Nucleation of  
13 nanometer-scale electrocatalyst particles in solid oxide fuel cell anodes. *J. Power Sources* **166**,  
14 64–67 (2007).
- 15 21. Kobsiriphat, W., Madsen, B. D., Wang, Y., Marks, L. D. & Barnett, S. A.  
16 La<sub>0.8</sub>Sr<sub>0.2</sub>Cr<sub>1-x</sub>Ru<sub>x</sub>O<sub>3-δ</sub>-Gd<sub>0.1</sub>Ce<sub>0.9</sub>O<sub>1.95</sub> solid oxide fuel cell anodes: Ru precipitation  
17 and electrochemical performance. *Solid State Ion.* **180**, 257–264 (2009).
- 18 22. Kobsiriphat, W. *et al.* Nickel- and Ruthenium-Doped Lanthanum Chromite Anodes: Effects  
19 of Nanoscale Metal Precipitation on Solid Oxide Fuel Cell Performance. *J. Electrochem. Soc.*  
20 **157**, B279–B284 (2010).
- 21 23. Bierschenk, D. M. *et al.* Pd-substituted (La,Sr)CrO<sub>3-δ</sub>-Ce<sub>0.9</sub>Gd<sub>0.1</sub>O<sub>2-δ</sub> solid oxide fuel cell  
22 anodes exhibiting regenerative behavior. *J. Power Sources* **196**, 3089–3094 (2011).



- 1 24. Adijanto, L., Padmanabhan, V. B., Kungas, R., J. Gorte, R. & M. Vohs, J. Transition metal-  
2 doped rare earth vanadates: a regenerable catalytic material for SOFC anodes. *J. Mater. Chem.*  
3 **22**, 11396–11402 (2012).
- 4 25. Neagu, D. *et al.* Demonstration of chemistry at a point through restructuring and catalytic  
5 activation at anchored nanoparticles. *Nat. Commun.* **8**, 1–8 (2017).
- 6 26. Sengodan, S. *et al.* Self-Decorated MnO Nanoparticles on Double Perovskite Solid Oxide Fuel  
7 Cell Anode by in Situ Exsolution. *ACS Sustain. Chem. Eng.* **5**, 9207–9213 (2017).
- 8 27. Kyriakou, V. *et al.* Co-electrolysis of H<sub>2</sub>O and CO<sub>2</sub> on exsolved Ni nanoparticles for efficient  
9 syngas generation at controllable H<sub>2</sub>/CO ratios. *Appl. Catal. B Environ.* **258**, 117950 (2019).
- 10 28. Zhu, C. *et al.* Electrochemical conversion of methane to ethylene in a solid oxide electrolyzer.  
11 *Nat. Commun.* **10**, 1–8 (2019).
- 12 29. Hou, N. *et al.* A-Site Ordered Double Perovskite with in Situ Exsolved Core–Shell  
13 Nanoparticles as Anode for Solid Oxide Fuel Cells. *ACS Appl. Mater. Interfaces* **11**, 6995–  
14 7005 (2019).
- 15 30. Thalinger, R. *et al.* Ni–perovskite interaction and its structural and catalytic consequences in  
16 methane steam reforming and methanation reactions. *J. Catal.* **337**, 26–35 (2016).
- 17 31. Singh, S. *et al.* Role of 2D and 3D defects on the reduction of LaNiO<sub>3</sub> nanoparticles for  
18 catalysis. *Sci. Rep.* **7**, (2017).
- 19 32. Hosseini, D. *et al.* Reversible Exsolution of Dopant Improves the Performance of Ca<sub>2</sub>Fe<sub>2</sub>O<sub>5</sub>  
20 for Chemical Looping Hydrogen Production. *ACS Appl. Mater. Interfaces* **11**, 18276–18284  
21 (2019).

- 1 33. Dimitrakopoulos, G., Ghoniem, A. F. & Yildiz, B. *In situ* catalyst exsolution on perovskite  
2 oxides for the production of CO and synthesis gas in ceramic membrane reactors. *Sustain.*  
3 *Energy Fuels* **3**, 2347–2355 (2019).
- 4 34. Kousi, K., Neagu, D., Bekris, L., Papaioannou, E. & Metcalfe, I. S. Endogenous Nanoparticles  
5 Strain Perovskite Host Lattice Providing Oxygen Capacity and Driving Oxygen Exchange and  
6 CH<sub>4</sub> Conversion to Syngas. *Angew. Chem. Int. Ed.* **n/a**,
- 7 35. Zhu, Y. *et al.* Synergistically enhanced hydrogen evolution electrocatalysis by in situ  
8 exsolution of metallic nanoparticles on perovskites. *J. Mater. Chem. A* **6**, 13582–13587 (2018).
- 9 36. Neagu, D. *et al.* *In Situ* Observation of Nanoparticle Exsolution from Perovskite Oxides: From  
10 Atomic Scale Mechanistic Insight to Nanostructure Tailoring. *ACS Nano* **13**, 12996–13005  
11 (2019).
- 12 37. Han, H. *et al.* Lattice strain-enhanced exsolution of nanoparticles in thin films. *Nat. Commun.*  
13 **10**, 1471 (2019).
- 14 38. Chen, Y. *et al.* Exceptionally active iridium evolved from a pseudo-cubic perovskite for  
15 oxygen evolution in acid. *Nat. Commun.* **10**, 1–10 (2019).
- 16 39. Yan, B. *et al.* Highly active subnanometer Rh clusters derived from Rh-doped SrTiO<sub>3</sub> for CO<sub>2</sub>  
17 reduction. *Appl. Catal. B Environ.* **237**, 1003–1011 (2018).
- 18 40. Lv, H. *et al.* In situ exsolved FeNi<sub>3</sub> nanoparticles on nickel doped Sr<sub>2</sub>Fe<sub>1.5</sub>Mo<sub>0.5</sub>O<sub>6-δ</sub>  
19 perovskite for efficient electrochemical CO<sub>2</sub> reduction reaction. *J. Mater. Chem. A* **7**, 11967–  
20 11975 (2019).
- 21 41. Sun, Y.-F. *et al.* Toward a rational photocatalyst design: a new formation strategy of co-  
22 catalyst/semiconductor heterostructures via in situ exsolution. *Chem. Commun.* **54**, 1505–1508  
23 (2018).

- 1 42. Wang, J. *et al.* Exsolution Synthesis of Nanocomposite Perovskites with Tunable Electrical  
2 and Magnetic Properties. *Adv. Funct. Mater.* 2108005 (2021).
- 3 43. Kwon, O. *et al.* Exsolution trends and co-segregation aspects of self-grown catalyst  
4 nanoparticles in perovskites. *Nat. Commun.* **8**, 15967 (2017).
- 5 44. Götsch, T. *et al.* Structural investigations of  $\text{La}_{0.6}\text{Sr}_{0.4}\text{FeO}_{3-\delta}$  under reducing conditions:  
6 kinetic and thermodynamic limitations for phase transformations and iron exsolution  
7 phenomena. *RSC Adv.* **8**, 3120–3131 (2018).
- 8 45. Thalinger, R., Gocyla, M., Heggen, M., Klötzer, B. & Penner, S. Exsolution of Fe and SrO  
9 Nanorods and Nanoparticles from Lanthanum Strontium Ferrite  $\text{La}_{0.6}\text{Sr}_{0.4}\text{FeO}_{3-\delta}$  Materials  
10 by Hydrogen Reduction. *J. Phys. Chem. C* **119**, 22050–22056 (2015).
- 11 46. Jo, Y.-R. *et al.* Growth Kinetics of Individual Co Particles Ex-solved on  $\text{SrTi}_{0.75}\text{Co}_{0.25}\text{O}_{3-\delta}$   
12 Polycrystalline Perovskite Thin Films. *J. Am. Chem. Soc.* **141**, 6690–6697 (2019).
- 13 47. Joo, S. *et al.* Cation-swapped homogeneous nanoparticles in perovskite oxides for high power  
14 density. *Nat. Commun.* **10**, 1–9 (2019).
- 15 48. Oh, T.-S. *et al.* Evidence and Model for Strain-Driven Release of Metal Nanocatalysts from  
16 Perovskites during Exsolution. *J. Phys. Chem. Lett.* **6**, 5106–5110 (2015).
- 17 49. Gao, Y. *et al.* Energetics of Nanoparticle Exsolution from Perovskite Oxides. *J. Phys. Chem.*  
18 *Lett.* **9**, 3772–3778 (2018).
- 19 50. Kim, K. J. *et al.* Facet-Dependent *in Situ* Growth of Nanoparticles in Epitaxial Thin Films:  
20 The Role of Interfacial Energy. *J. Am. Chem. Soc.* **141**, 7509–7517 (2019).
- 21 51. Zubenko, D., Singh, S. & Rosen, B. A. Exsolution of Re-alloy catalysts with enhanced stability  
22 for methane dry reforming. *Appl. Catal. B Environ.* **209**, 711–719 (2017).

- 1 52. Katz, M. B. *et al.* Reversible precipitation/dissolution of precious-metal clusters in perovskite-  
2 based catalyst materials: Bulk versus surface re-dispersion. *J. Catal.* **293**, 145–148 (2012).
- 3 53. Dai, S., Zhang, S., Katz, M. B., Graham, G. W. & Pan, X. *In Situ* Observation of Rh-CaTiO<sub>3</sub>  
4 Catalysts during Reduction and Oxidation Treatments by Transmission Electron Microscopy.  
5 *ACS Catal.* **7**, 1579–1582 (2017).
- 6 54. Chiu, I.-T. *et al.* Cation and anion topotactic transformations in cobaltite thin films leading to  
7 Ruddlesden-Popper phases. *Phys. Rev. Mater.* **5**, 064416 (2021).
- 8 55. Li, J. *et al.* Topotactic phase transformations by concerted dual-ion migration of B-site cation  
9 and oxygen in multivalent cobaltite La–Sr–Co–Ox films. *Nano Energy* **78**, 105215 (2020).
- 10 56. Kousi, K., Neagu, D., Bekris, L., Papaioannou, E. I. & Metcalfe, I. S. Endogenous  
11 Nanoparticles Strain Perovskite Host Lattice Providing Oxygen Capacity and Driving Oxygen  
12 Exchange and CH<sub>4</sub> Conversion to Syngas. *Angew. Chem.* **132**, 2531–2540 (2020).
- 13 57. Cliff, G. & Lorimer, G. W. The quantitative analysis of thin specimens. *J. Microsc.* **103**, 203–  
14 207 (1975).
- 15 58. Lorimer, G. W. Quantitative X-ray microanalysis of thin specimens in the transmission  
16 electron microscope; a review. *Mineral. Mag.* **51**, 49–60 (1987).
- 17 59. Bowman, W. J., Darbal, A. & Crozier, P. A. Linking Macroscopic and Nanoscopic Ionic  
18 Conductivity: A Semiempirical Framework for Characterizing Grain Boundary Conductivity  
19 in Polycrystalline Ceramics. *ACS Appl. Mater. Interfaces* **12**, 507–517 (2020).
- 20 60. Sohlberg, K., J. Pennycook, T., Zhou, W. & J. Pennycook, S. Insights into the physical  
21 chemistry of materials from advances in HAADF-STEM. *Phys. Chem. Chem. Phys.* **17**, 3982–  
22 4006 (2015).
- 23 61. Pennycook, S. J. Z-contrast stem for materials science. *Ultramicroscopy* **30**, 58–69 (1989).

- 1 62. Yu, S. *et al.* Metal Nanoparticle Exsolution on a Perovskite Stannate Support with High  
2 Electrical Conductivity. *Nano Lett.* **20**, 3538–3544 (2020).
- 3 63. Howell, P. G. T., Davy, K. M. W. & Boyde, A. Mean atomic number and backscattered  
4 electron coefficient calculations for some materials with low mean atomic number. *Scanning*  
5 **20**, 35–40 (1998).
- 6 64. Ruddlesden, S. N. & Popper, P. The compound  $\text{Sr}_3\text{Ti}_2\text{O}_7$  and its structure. *Acta Crystallogr.*  
7 **11**, 54–55 (1958).
- 8 65. Suzuki, T., Nishi, Y. & Fujimoto, M. Defect structure in homoepitaxial non-stoichiometric  
9 strontium titanate thin films. *Philos. Mag. A* **80**, 621–637 (2000).
- 10